

Nearly 90% Circularly Polarized Emission in Monolayer WS₂ Single Crystals by Chemical Vapor Deposition

Wei-Hsiang Lin,[†] Wei-Shiuan Tseng,[‡] Cora M. Went,[‡] Marcus L. Teague,[‡] George R. Rossman,[§] Harry A. Atwater,^{†,||} and Nai-Chang Yeh^{*,‡,||}

[†]Department of Applied Physics, California Institute of Technology, Pasadena, California 91125, United States

[‡]Department of Physics, California Institute of Technology, Pasadena, California 91125, United States

[§]Division of Geological and Planetary Sciences, California Institute of Technology, Pasadena, California 91125, United States

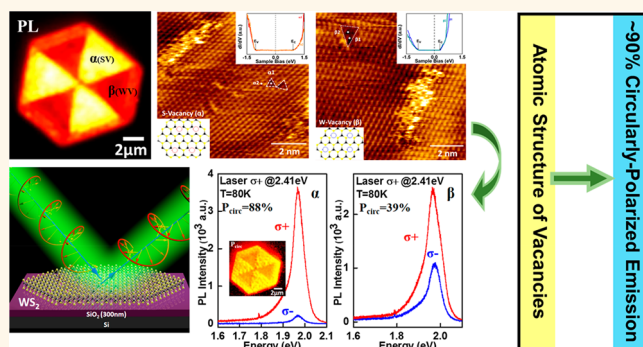
^{||}Kavli Nanoscience Institute, California Institute of Technology, Pasadena, California 91125, United States

Supporting Information

ABSTRACT: Monolayer transition-metal dichalcogenides (TMDCs) in the 2H-phase are promising semiconductors for opto-valleytronic and opto-spintronic applications because of their strong spin-valley coupling. Here, we report detailed studies of opto-valleytronic properties of heterogeneous domains in CVD-grown monolayer WS₂ single crystals. By illuminating WS₂ with off-resonance circularly polarized light and measuring the resulting spatially resolved circularly polarized emission (P_{circ}), we find significantly large circular polarization (P_{circ} up to 60% and 45% for α - and β -domains, respectively) already at 300 K, which increases to nearly 90% in the α -domains at 80 K. Studies of spatially resolved photoluminescence (PL)

spectroscopy, Raman spectroscopy, X-ray photoelectron spectroscopy, Kelvin-probe force microscopy, and conductive atomic force microscopy reveal direct correlation among the PL intensity, defect densities, and chemical potential, with the α -domains showing lower defect densities and a smaller work function by 0.13 eV than the β -domains. This work function difference indicates the occurrence of type-two band alignments between the α - and β -domains. We adapt a classical model to explain how electronically active defects may serve as nonradiative recombination centers and find good agreement between experiments and the model. Scanning tunneling microscopic/spectroscopic (STM/STS) studies provide further evidence for tungsten vacancies (WVs) being the primary defects responsible for the suppressed PL and circular polarization in WS₂. These results therefore suggest a pathway to control the opto-valleytronic properties of TMDCs by means of defect engineering.

KEYWORDS: transition metal dichalcogenides, WS₂, CVD, KPFM, CAFM, STM, valley polarization



Atomic Structure of Vacancies
~90% Circularly-Polarized Emission

There has been a surge of intense research efforts on two-dimensional (2D) van der Waals (vdW) materials because of their interesting properties and great promise for technological applications.^{1–4} These 2D materials, such as semimetallic graphene,^{5–9} insulating h-BN,^{10–14} and semiconducting transition-metal dichalcogenides (TMDCs),^{15–19} can be synthesized on a wafer scale by chemical vapor deposition (CVD), which provides a feasible route toward practical applications. The electrical and optical properties of TMDCs can be significantly affected by crystal imperfections such as vacancies, impurities, and grain boundaries.^{20–22} In particular, vacancies in TMDCs appear to be unpreventable and are naturally formed inside the single crystalline grains during the CVD growth process. Such

vacancies can be primary contributors to carrier scattering, doping effects, and varying optical properties in these materials.

Among TMDCs in the 2H-phase, monolayer tungsten disulfide (WS₂) consists of a plane of tungsten atoms sandwiched between top and bottom sulfur layers. It has been found that atomic vacancies of tungsten and sulfur are common occurrences in WS₂ and that the electrical and optical properties of a given WS₂ monolayer are dominated by the

Received: July 15, 2019

Accepted: August 23, 2019

Published: August 23, 2019

type of vacancies because of differences in the defect states. For instance, monolayer hexagonal-shape WS₂ (h-WS₂) flakes with triangular heterogeneous defect domains have been synthesized by CVD under hydrogen-rich growth conditions, as reported by several research groups.^{23–27} Curiously, the optical emission in the h-WS₂ flakes exhibits alternating areas of bright and dark photoluminescence (PL) emission within each h-WS₂ flake, and the resulting PL image looks similar to the radioactive hazard symbol, as exemplified by the left panel of Figure 1a. According to previous studies,^{23–27} the α -domains

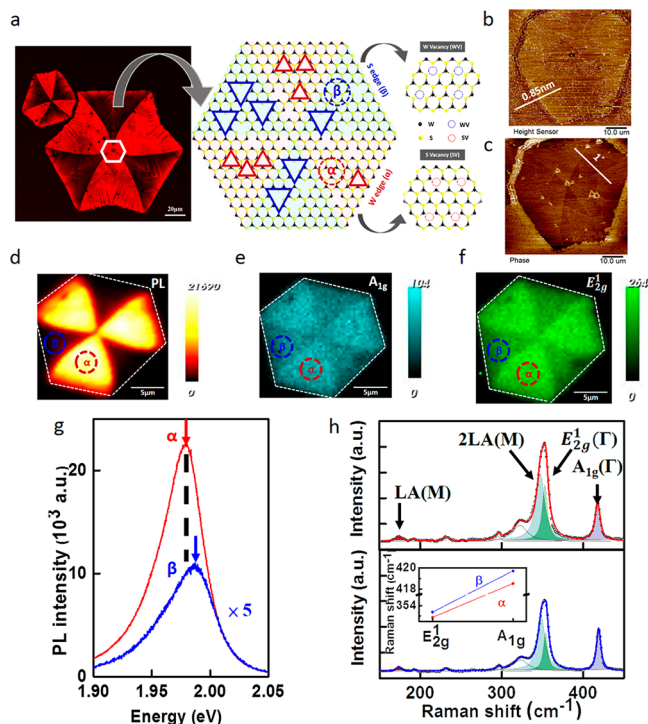


Figure 1. Monolayer h-WS₂ optical characterizations. (a) Left panel: Fluorescence images showing a radioactive hazard symbol-like optical emission pattern in the fluorescence intensity from a CVD-grown large monolayer WS₂ single crystal. Right panel: Schematic illustration of heterogeneous defect domains in single crystalline hexagonal WS₂. AFM measurements of (b) the surface topography and (c) the phase for a monolayer h-WS₂ single crystal. The scale bar is 10 μ m. (d) PL intensity mapping of a monolayer h-WS₂ single crystal at the PL peak energy of 1.96 eV. The brighter PL domain (α) and darker PL domain (β) show 3-fold symmetry. Similar symmetries are also found in the Raman spectral intensity mapping for (e) the A_{1g} mode and (f) the E_{2g} mode. Here the scale bars for (d–f) correspond to 5 μ m. (g) Representative PL point spectra for the α - and β -domains of a monolayer h-WS₂. (h) Representative Raman spectra for the corresponding α - and β -domains as in (e) and (f).

with a stronger PL intensity and higher mobility are associated with W-edges and S-vacancies (SVs), and the β -domains with a significantly quenched PL intensity and lower electron mobility exhibit a blue-shifted PL peak position and are associated with S-edges and W-vacancies (WVs). A schematic illustration of the heterogeneous defect domains for WVs and SVs in a single-crystalline h-WS₂ is shown in the right panel of Figure 1a.

Similar to other monolayer TMDCs in the 2H-phase, monolayer WS₂ is an ideal candidate for valleytronic applications due to its inequivalent K and K' valleys at the edge of the Brillouin zone.^{28,29} Because of strong spin–orbit

coupling and time-reversal symmetry, the valence bands (VB) in the K (K') valley have a large energy spin splitting of \sim 420 meV for WS₂^{28,29} between the top spin-up (spin-down) band and the bottom spin-down (spin-up) band. This difference results in valley-dependent optical selection rules: circularly polarized light with positive helicity ($\sigma+$) couples to the K valley and the negative helicity ($\sigma-$) couples to the K' valley.^{30–32} It is therefore possible to selectively populate and manipulate the different valleys (K or K') by means of circularly polarized light.

When monolayer WS₂ is illuminated with circularly polarized light of photon energies larger than the energy gap, excitons (*i.e.*, bound electron–hole pairs) are created in a single valley. The radiative decay of excitons within this valley subsequently generates circularly polarized light due to the optical selection rules. Therefore, measuring the circular polarization of photoluminescence (PL) provides a direct means to monitor the valley population. Valley populations will also be affected by intervalley scattering, a process that may be enabled by Coulomb interactions or impurity/phonon scattering.^{33–36} At high temperatures or under a sufficiently high photon-excitation energy, large phonon populations will couple to the valleys, thereby reducing the valley-specific populations. To date, most reports of circularly polarized PL spectra^{37–41} have only been observed in systems measured at relatively low temperatures (<30 K) or near the resonant excitation condition.

Here, we report successful CVD growth (Figure S1) of monolayer h-WS₂ that exhibits significant circular polarization already at room temperature and nearly 90% circular polarization (CP) in the α -domains at 80 K without the resonant excitation conditions. Detailed characterizations by Raman spectroscopy, PL, X-ray photoemission spectroscopy (XPS), and conducting atomic force microscopy (CAFM) revealed that these h-WS₂ samples were of high quality, large domains and low defect densities. Additionally, systematic studies of monolayer h-WS₂ by spatially resolved PL maps and point spectra of polarized PL emission were made on the α - and β -domains of h-WS₂ at both room temperature and low temperature (80 K). We found that at room temperature the PL spectra of neutral excitons exhibited a CP of \sim 50% and \sim 40% in the α - and β -domains, respectively. Moreover, the degree of circularly polarized emission in α -domains approached \sim 90% at 80 K, suggesting nearly perfect valley polarization. Spatially resolved CAFM studies revealed that the areal defect density was on the order of 10^{10} cm⁻² in the α -domains and on the order of 10^{11} cm⁻² in the β -domains. Following a similar analysis in refs 42 and 51, we related the areal defect density in each domain to the corresponding PL intensity and obtained an estimate for the nonradiative recombination lifetime.^{42,51} Additionally, spatially resolved studies using Kelvin-probe force microscopy (KPFM) found that the work function in the β -domains was consistently larger than that in the α -domains by 0.15 eV, suggesting type-2 semiconducting band alignments along the domain boundaries that are favorable for stabilizing interfacial excitons.⁵² Atomically resolved imaging and spectroscopic studies by scanning tunneling microscopy (STM) further revealed that the nonradiative defects were primarily associated with the WVs rather than SVs, consistent with the CAFM findings in regions of higher defect densities. Our results thus provide direct evidence for WVs being the primary nonradiative recombina-

tion sites in h-WS₂ that are responsible for the suppression of PL intensity and circular polarization.

RESULTS AND DISCUSSION

Monolayer h-WS₂ samples were synthesized on SiO₂ (300 nm)/Si substrates by means of CVD, as schematically shown in Figure S1 and S2. The hexagonal flakes typically had lateral dimensions on the order of several tens to hundreds of micrometers so that optical studies at many discrete locations across a single flake could be carried out. Further details for the h-WS₂ growth processes are described in the Methods and Supporting Information Note 1.

Our monolayer h-WS₂ samples exhibited typical fluorescence images analogous to the radioactive hazard symbol, as mentioned in the introduction and exemplified in Figure 1a. Spatially resolved topographic studies on the same samples using atomic force microscopy (AFM) revealed smooth topographic maps (Figure 1b). Specifically, while the height difference between the WS₂ single crystal and the SiO₂/Si substrate was ~ 0.85 nm, which was consistent with the monolayer thickness of WS₂, there was no discernible height differences between the two domains of different PL intensities (Figure 1d). Spatially resolved measurements of the AFM phase mode revealed a clear phase difference (1°) between the two domains (Figure 1c), and the resulting phase map correlated well with the pattern shown in Figure 1d. Similarly, spatially resolved Raman spectroscopic maps for the A_{1g} and E_{2g}¹ modes of a monolayer h-WS₂ single crystal (shown, respectively, in Figure 1e, f) also exhibited the same pattern.

Figure 1g shows a representative PL spectrum from 1.96 to 2.01 eV for the typical A-exciton peak of h-WS₂. The A-exciton PL peak for the α -domain is red-shifted compared to that of the β -domain. This redshift may be attributed to tensile strain existed in the α -domains and/or to a higher carrier density. Moreover, the PL intensity in the α -domains is always enhanced by about 1 order of magnitude when compared with the β -domains.

Generally speaking, the PL intensity can be modulated by a variety of factors such as stoichiometry, strain, doping, and density of nonradiative recombination centers. To investigate the contributions from strain and doping effects, we performed Raman intensity and frequency mapping of the A_{1g} and E_{2g}¹ modes, which displayed contrast between the α - and β -domains (Figure 1e,f) and were similar to the PL mapping (Figure 1d). We found that the strain-related E_{2g}¹ mode exhibited a redshift in the α -domain relative to the β -domain (0.5 cm⁻¹), indicating a tensile-strain effect. Similarly, the redshift (1.2 cm⁻¹) of the doping-related A_{1g} mode in the α -domain relative to the β -domain implied carrier doping effects (Figure 1h), which was consistent with the observed PL redshift (Figure 1g). The LA (M) mode at 176 cm⁻¹, which is associated with the longitudinal acoustic phonon at the M point of the Brillouin zone, may be considered as a useful indicator of the sample quality. Specifically, a finite intensity of the LA (M) mode implies the presence of defects or disorder that satisfied the $q = 0$ Raman selection rule. Additionally, the intensity of the LA (M) mode, $I(\text{LA})$, may be related to the interdefect spacing (L_D)⁴³ by the expression $I(\text{LA}) \propto L_D^{-2}$. Figure S3 demonstrates that the intensity of the LA (M) mode associated with the β -domain was shown to be larger than that of the α -domain, implying a shorter interdefect distance and therefore a higher areal density of disorder in the β -domain

that signifies more nonradiative recombination centers and a reduced PL intensity.

In addition to the PL/Raman spectroscopic studies, spatially resolved X-ray photoelectron emission spectroscopy (XPS) was carried out on monolayer WS₂ transferred to Au (111)/mica substrates (Figure 2a) to probe the chemical composition

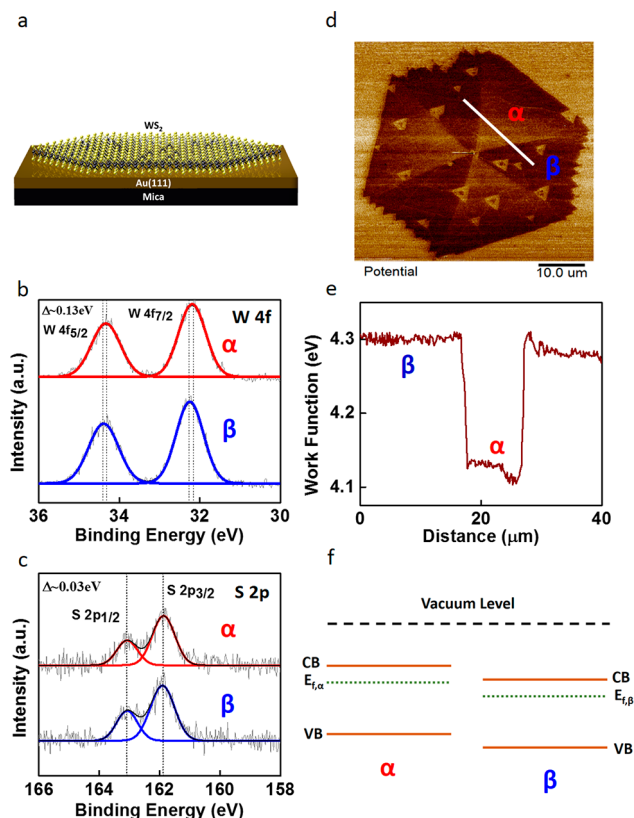


Figure 2. Chemical bonding and work function characterization in heterogeneous domains: (a) Schematic of the monolayer h-WS₂ on Au (111)/mica substrate. Selected XPS spectra of the α -domain (top) and β -domain (bottom) for (b) W-4f and (c) S-2p, showing an upshift by ~ 0.13 eV (~ 0.03 eV) in the W-4f (S-2p) peaks of the α -domain relative to those of the β -domain. The error range for the binding energies determined by our XPS system is ± 0.025 eV. (d) KPFM image of the heterogeneous domains of a monolayer h-WS₂. (e) Work function plot along the white line in (d). (f) Estimated Fermi levels ($E_{f,\alpha}$ and $E_{f,\beta}$) and the corresponding conduction band (CB) and valence band (VB) positions of the α - and β -domains with respect to the vacuum level based on KPFM.

and stoichiometry of the h-WS₂ single crystal. High-resolution XPS mapping performed on the h-WS₂ samples revealed apparent hexagonal geometry, as exemplified in Figure S4a. Photoelectrons from core level of W and S atoms were acquired from both α - and β -domains. As shown in Figure 2b,c, the corresponding binding energies in the α -domain (β -domain) were 34.31 eV (34.44 eV) for W_{4f}_{5/2}, 32.15 eV (32.28 eV) for W_{4f}_{7/2}, 162.87 eV (162.9 eV) for S_{2p}_{3/2}, and 163.07 eV (163.1 eV) for S_{2p}_{1/2}. Considering the error range of ± 0.025 eV for the binding energies determined using our XPS system, the upshift in the α -domain binding energies (~ 0.13 eV) relative to those in the β -domain was prominent for the W-4f peaks, in good agreement with the valence-band maximum shift due to doping-induced Fermi level modulation. In contrast, the upshift of the S-2p peaks (~ 0.03 eV) was much

smaller and essentially negligible given the error range of our XPS system. This negligible upshift of the S-2p peaks in the α -domain may be attributed to the tensile strain effect that affected the S-2p valence electrons more significantly, which contributed to a binding-energy downshift that compensated the doping-induced binding energy upshift. On the other hand, the tensile strain had much weaker effects on the W-4f core electrons so that the doping-induced energy upshifts prevailed for the W-4f peaks in the α -domain.

We have also explored the surface potential (work function) of the α - and β -domains by means of KPFM because the work functions of semiconductor 2D materials are sensitive to the corresponding variable Fermi level. To determine the work function of the Al-coated AFM tip, we first performed ultraviolet photoemission spectroscopy (UPS) measurements on the Au (111)/mica sample, which found the work function of Au (111) to be 4.8 eV, as shown in Figure S4b. Next, we performed KPFM measurements using the Al-coated AFM tip on Au (111)/mica, which yielded the value of the contact potential difference (V_{CPD}^0) between the Al-coated AFM tip and Au (111), where the contact potential difference (V_{CPD}^0) was defined as the difference between the work function of the tip (ϕ_{tip}^0) and that of Au (111), so that $eV_{\text{CPD}}^0 = \phi_{\text{tip}}^0 - 4.8$ eV. Finally, KPFM measurements using the Al-coated AFM tip on h-WS₂ yielded the contact potential difference (V_{CPD}) between the Al-coated AFM tip and different domains of the h-WS₂ sample so that we obtained the following relationship

$$eV_{\text{CPD}} = \phi_{\text{tip}} - \phi_{\text{WS}_2} \Rightarrow \phi_{\text{WS}_2} = \phi_{\text{tip}} - eV_{\text{CPD}} \quad (1)$$

where ϕ_{WS_2} is the work function of the WS₂ sample. From spatially resolved measurements of V_{CPD} , the work function difference between the α - and β -domains can be determined, and the resulting KPFM images are shown in Figures 2d,e.

A schematic representation of the band diagram with the Fermi levels for the α - and β -domains relative to the vacuum level is shown in Figure 2f. The difference in the Fermi levels between the α - and β -domains can be calculated directly from V_{CPD} using the following equation

$$\begin{aligned} \Delta E_f &= E_{f,\alpha} - E_{f,\beta} = eV_{\text{CPD},\alpha} - eV_{\text{CPD},\beta} = e\Delta V_{\text{CPD}} \\ &= (\phi_\beta - \phi_\alpha) \end{aligned} \quad (2)$$

where $E_{f,\alpha}(\phi_\alpha)$ and $E_{f,\beta}(\phi_\beta)$ are the Fermi levels (work functions) of the α - and β -domains, respectively. Interestingly, we note that the band diagram at the interface of the α - and β -domains is consistent with a type-2 band alignment that supports long-lived interfacial excitons.⁵²

To investigate the degree of valley polarization in our monolayer h-WS₂, we performed polarization-resolved PL spectroscopy measurements at both room temperature and 80 K under the excitation of a 514 nm continuous-wave laser source, as schematically illustrated in Figure 3a.

For spatially resolved PL mapping, the sample was excited with σ_+ helicity, and the laser was scanned across a (13 μm \times 13 μm) area at a step size of 0.2 μm . The detection optics were set first for the σ_+ analysis and then for the σ_- analysis over the same area in two separate scans. The energy of the PL peak within the range of 1.9 to 2.1 eV for the σ_+ (σ_-) detection was determined, and the PL intensity map taken at the peak energy is shown in Figure 3b for the σ_+ detection and in Figure 3c for the σ_- detection, both obtained at room temperature (RT). These PL maps reveal the same emission pattern as the

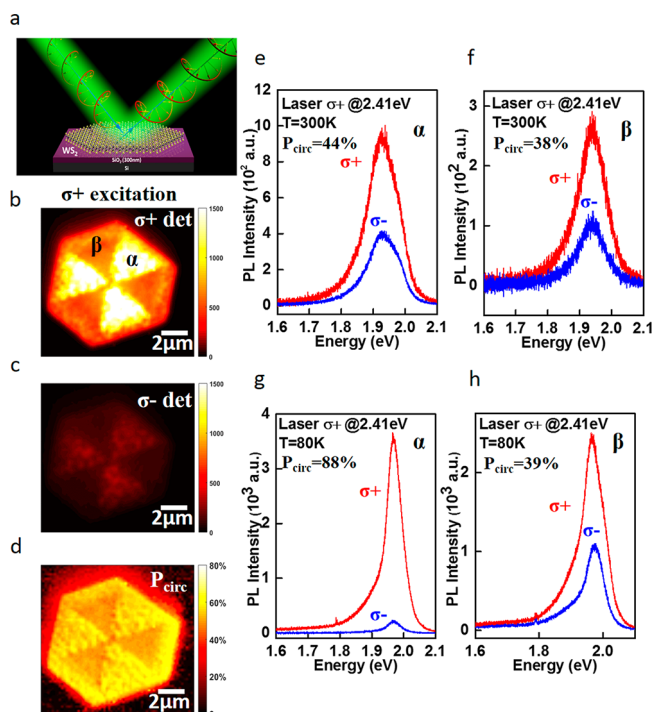


Figure 3. Circularly polarized emission of monolayer h-WS₂ neutral excitons: (a) Schematic of circularly polarized emission on monolayer h-WS₂ under σ_+ 514 nm (2.41 eV) excitation. (b) Intensity map for the σ_+ polarized emission and (c) an intensity map for the σ_- polarized emission. (d) A spatial map for the degree of valley polarization P_{circ} in a monolayer h-WS₂ single crystal. (e, f) Representative σ_+ (red) and σ_- (blue) PL intensity spectra taken at room temperature on the α - and β -domains, respectively. (g–h) Representative σ_+ (red) and σ_- (blue) PL intensity spectra taken at 80 K on the α - and β -domains, respectively.

unpolarized excitation. This type of PL pattern, with lower PL intensity in the β -domain and higher PL intensity in the α -domain (about 10 times stronger than that in the β -domain) was common among all monolayer h-WS₂ single crystals that we synthesized.

Given the polarization-resolved PL intensities $I(\sigma_+)$ and $I(\sigma_-)$, the degree of circular polarization (P_{circ}) is defined by the following expression:

$$P_{\text{circ}} = \frac{I(\sigma_+) - I(\sigma_-)}{I(\sigma_+) + I(\sigma_-)} \quad (3)$$

Using eq 3, the degree of circular polarization across a monolayer h-WS₂ crystal was obtained and is illustrated in Figure 3d. The higher degree of polarization (DOP) in the α -domain (45–60%) and lower DOP in the β -domain (20–45%) was found to be well correlated to the PL intensity pattern. Similar results were also obtained for polarization-resolved mapping acquired with the σ_- excitation, as shown in Figure S5.

The PL spectra of the α -domain (Figure 3e) and the β -domain (Figure 3f) taken at RT both displayed a single peak with the maximum intensity at 1.92 eV, indicating that the RT emission characteristics were dominated by the neutral excitons. These neutral excitons exhibited very large circular polarization at both the α -domain ($P_{\text{circ}} \sim 50\%$) and β -domain ($P_{\text{circ}} \sim 40\%$) of our h-WS₂ samples even at RT, in stark

contrast to recent reports by other groups (with $P_{\text{circ}} = 0.2\text{--}32\%$) on monolayer WS_2 ,^{40–42} as summarized in Table S2. The PL peak for both domains was found to slightly blue-shift to 1.96 eV at a lower temperature (LT) 80 K. As exemplified in Figure 3g, the LT (80 K) PL intensity of the σ_+ detection at the α -domain increased 3-fold relative to the corresponding RT signals, whereas the PL intensity of the σ_- detection remained the same at 80 K. In particular, the DOP at the α -domain approached nearly 90% at 80 K. In contrast, the LT (80K) PL spectra at the β -domain revealed that the PL intensities for both the σ_+ and σ_- detections increased 10-fold relative to the corresponding PL spectra at RT, as exemplified by Figure 3h. However, the DOP of the β -domain at 80 K remained largely the same as that at RT.

Our finding of significant disparity in the DOP enhancement with decreasing temperature for two different domains is quite unusual: while the common observation of increasing PL intensity with decreasing temperature may be attributed to the reduction of thermally activated nonradiative recombination, this mechanism should have resulted in a comparable enhancement factor with decreasing temperature for the PL intensity in the same material. However, the enhancement factor for the PL intensity at LT was apparently different in different domains of the h- WS_2 single crystal, which led to significantly different DOP at LT. A feasible explanation for such disparity in the DOP enhancement with decreasing temperature may be due to negligible nonradiative recombination centers for excitons in the α -domain as opposed to more nonradiative recombination centers in the β -domain. To shed light on this issue, we performed spatially resolved conductive atomic force microscope (CAFM) measurements to be detailed below, which facilitated precise identifications of defects that could serve as the nonradiative recombination centers and also provided direct quantifications of the areal defect density.

A schematic illustration of the experimental configuration for the CAFM measurements is shown in Figure 4a, where all data acquisition was done at RT in air. It is worth noting that careful sample preparation for the CAFM measurements was critically important to obtaining reproducible results. In particular, an atomically flat conductive substrate for the monolayer h- WS_2 sample was necessary. For this purpose, we first transferred a thick piece of CVD-grown graphite onto an atomically flat Au (111) (200 nm)/mica substrate, followed by a monolayer of h- WS_2 transferred from its CVD growth substrate onto the graphite/Au (111)/mica substrate. After the transfer, we annealed the combined sample-on-substrate in a hydrogen–argon gas mixture (with a ratio of H_2 to Ar of 1–3) for 3 h to remove possible contaminants and wrinkles, which helped improve the contact uniformity between the monolayer h- WS_2 and the graphite substrate. Details of the h- WS_2 transfer and the annealing processes can be found in the Methods and Supporting Information. Lastly, a voltage was applied to the sample lead so that a current flowed between the Pt/Ir coated CAFM tip and the sample, and this current was recorded by a current amplifier. By scanning the AFM tip across the sample and recording the currents at each pixel with a pixel spacing of 0.9 nm, we obtained spatially resolved CAFM maps over different domains of the h- WS_2 sample.

In these CAFM maps, the locations of defects were easily identified as distinct high-current features: the defect locations generally exhibited more than 2 orders of magnitude higher currents than areas without defects. Additionally, the electrical

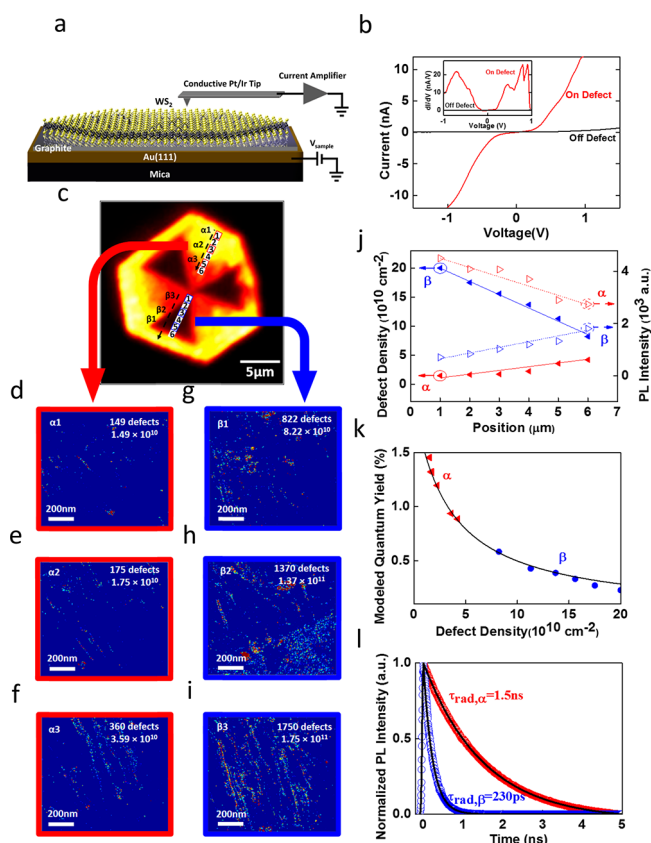


Figure 4. Electrical characterizations of the monolayer h- WS_2 : (a) Schematic illustration of the experimental setup for the CAFM measurements. A CVD-grown thick multilayer graphene sample was transferred onto an atomically flat Au (111)/mica substrate to provide a conductive backplane for the measurement. A monolayer h- WS_2 sample was subsequently transferred onto the thick multilayer graphene using the transfer method described in the Methods. (b) I – V curves taken on a defect and off a defect, showing a drastic difference in the conduction characteristics between a defect region and the pristine h- WS_2 . The inset figure in (b) shows the dI/dV characteristics corresponding to the I – V curve in the main panel of (b). (c) PL map of the h- WS_2 sample, with numbers 1–6 labeled in both one of the α -domains and one of the β -domains. The numbers correspond to the locations where detailed CAFM maps were taken. (d–i) CAFM measurements of the locations (α_1 , α_2 , α_3 , β_1 , β_2 , β_3) labeled in (c), exhibiting defect densities in the α -domain: (d) $1.49 \times 10^{10} \text{ cm}^{-2}$ for α_1 , (e) $1.75 \times 10^{10} \text{ cm}^{-2}$ for α_2 , (f) $3.59 \times 10^{10} \text{ cm}^{-2}$ for α_3 , and in the β -domain: (g) $8.22 \times 10^{10} \text{ cm}^{-2}$ for β_1 , (h) $1.37 \times 10^{11} \text{ cm}^{-2}$ for β_2 , (i) $1.75 \times 10^{11} \text{ cm}^{-2}$ for β_3 . (j) Defect density and PL intensity as a function of position along the dashed line shown in (c) across the α - and β -domains, showing apparent anticorrelation between the defect density and the PL intensity. (k) Model presented in eq 7. The red points correspond to the PL measurements of the α -domain, and blue points correspond to the PL measurements of the β -domain. (l) TRPL results, showing PL decay profiles of the α - and β -domains. The black lines are fitting curves using a single exponential decay function.

characteristics of each defect could be well quantified by measurements of the current–voltage (I – V) curves, as exemplified in Figure 4b by the comparison of a typical I – V curve obtained on a defect with a reference I – V curve obtained away from any defects. The I – V curve associated with a defect exhibited much enhanced currents at bias voltages $|V| > 0.3 \text{ V}$ and was nearly symmetric about zero applied bias. These

defect sites were generally much more conductive than regions without defects, as demonstrated by the comparison of the differential conductance taken on and off defects in the inset of Figure 4b.

In Figure 4d–i, spatially resolved CAFM differential conductance maps taken at a bias voltage of 0.9 V are shown over different $1\ \mu\text{m} \times 1\ \mu\text{m}$ areas at locations specified on the h-WS₂ single crystal in Figure 4c, which shows a spatial map of PL intensity taken on the sample after its transfer onto the substrate for the CAFM measurements. The apparent visibility of defect locations in the CAFM maps enabled direct counting of the number of the defects in both the α - and β -domains. Specifically, for the α -domain, we found 149 defects in Figure 4d, which corresponded to a defect density of $1.49 \times 10^{10}\ \text{cm}^{-2}$. Similarly, we obtained 175 defects ($1.75 \times 10^{10}\ \text{cm}^{-2}$) in Figure 4e and 359 defects ($3.59 \times 10^{10}\ \text{cm}^{-2}$) in Figure 4f. For the β -domain, we found 822 defects ($8.22 \times 10^{10}\ \text{cm}^{-2}$) in Figure 4g, 1370 defects ($1.37 \times 10^{11}\ \text{cm}^{-2}$) in Figure 4h, and 1750 defects ($1.75 \times 10^{11}\ \text{cm}^{-2}$) in Figure 4i. These CAFM measurements clearly indicated that the areal density of these highly conductive defect sites was about 1 order of magnitude higher in the β -domain than in the α -domain.

Here, we emphasize that other types of defects not detectable by the CAFM measurements may exist, and in this work we only consider one specific type of defects that are most electrically active and correlate their densities with the corresponding spatially resolved PL. In Figure 4j we compare the defect density and the PL intensity as a function of the position numerated along a line in Figure 4c and find that the measured defect density generally anticorrelates with the PL intensity for both α - and β -domains.

A major challenge to understanding the excitonic behavior in h-WS₂ is the wide variety of mechanisms that can affect the exciton recombination, including substrate effects, defect related recombination and other nonradiative recombination pathways.^{44–51} From our experiments, the apparent anticorrelation between the defect density and the PL intensity is helpful in identifying the role of defects in the exciton recombination for monolayer h-WS₂.

Generally speaking, the PL intensity is proportional to the PL quantum yield (QY) of excitons, and a standard QY is defined by the following expression

$$\text{QY} \equiv \tau_r^{-1} / (\tau_r^{-1} + \tau_{\text{nr}}^{-1}) \quad (4)$$

where $\tau_r(\tau_{\text{nr}})$ is the average radiative (nonradiative) recombination time of excitons. Typically the nonradiative recombination rate τ_{nr}^{-1} may be further divided into two components if we assume that excitons do not interact with each other. That is

$$\tau_{\text{nr}}^{-1} = \tau_{\text{nr,sub}}^{-1} + \tau_{\text{nr,defect}}^{-1} \quad (5)$$

where $\tau_{\text{nr,sub}}$ is the average nonradiative recombination time for substrate related effects, which may also include any other nonradiative recombination mechanisms, and $\tau_{\text{nr,defect}}$ is the average nonradiative recombination time for defect-related effects.

To understand the correlation between the defect density and PL intensity, we followed a similar analysis by Rosenberger *et al.*⁴² Specifically, we assumed that the defect-related nonradiative recombination occurred when excitons collided with defects and resulted in nonradiative recombination. For an exciton with an effective collision radius r traveling with a

speed v , an area swept by the exciton over a time period t in the 2D sheet with a defect density n_d would result in N collisions, where $N = n_d(2rvt)$. Therefore, the collision time $\tau_{\text{nr,defect}}$ between the exciton and defects can be defined by the following expression:

$$\tau_{\text{nr,defect}} = \frac{t}{N} = \frac{t}{n_d(2rvt)} = \frac{1}{2rvn_d}, \Rightarrow \tau_{\text{nr,defect}}^{-1} = 2rvn_d \quad (6)$$

Combining eqs 4–6 and assuming that the QY and the empirical PL intensity, $(PL)_{\text{exp}}$, are related by a scaling coefficient C , we arrived at the following relation:⁴²

$$(PL)_{\text{exp}} = C \frac{\tau_r^{-1}}{\tau_r^{-1} + \tau_{\text{nr,sub}}^{-1} + 2rvn_d} \quad (7)$$

Empirically, the values of τ_r in different domains could be directly determined from time-resolved PL (TRPL), which yielded $\tau_r = 1.5\ \text{ns}$ in the α -domain and $\tau_r = 230\ \text{ps}$ in the β -domain for monolayer h-WS₂. These values were consistent with the range of 0.2–4 ns reported in the literature for monolayer WS₂.^{43,48,50} If we further assumed that a thermal speed of excitons at RT is $v = 10^5\ \text{m/s}$,^{53,54} and an effective collision radius $r = 2.1\ \text{nm}$ based on previous reports,⁵⁴ we obtained in Figure 4k the relation between the spatially varying PL intensity of a monolayer h-WS₂ on graphite/Au (111)/mica and the corresponding local defect density. The solid black line represents the fitting curve for the PL measurements using eq 7 with the fitting parameters $C = 3.1 \times 10^5$ and $\tau_{\text{nr,sub}} = 30\ \text{ps}$. These fitting parameters were consistent for both domains in h-WS₂, which implies that our direct quantification of the defect density n_d helped decouple the defect-related nonradiative recombination (associated with $\tau_{\text{nr,defect}}^{-1} = 2rvn_d$) from other nonradiative mechanisms (associated with $\tau_{\text{nr,sub}}^{-1}$).

To understand why the DOP differed in the α - and β -domains, we considered a rate equation model in the steady state to find the relationship between the DOP and defect-related nonradiative recombination. As detailed in Supporting Information Note 6, the circular polarization P_{circ} for neutral excitons in the steady-state rate model can be given by the following expression

$$P_{\text{circ}} = \frac{P_0(1 - \delta)^2}{1 + 2(\tau_{\text{ex}}/\tau_{\text{intervalley}})} = \frac{P_0[1 - (\delta_{\text{imp}} + \delta_{\text{phonon}})]}{1 + 2(\tau_{\text{ex}}/\tau_{\text{intervalley}})} \quad (8)$$

where P_0 is the theoretical degree of circular polarization, $\tau_{\text{ex}}(\tau_{\text{intervalley}})$ is the neutral exciton (intervalley) relaxation time, and $(1 - \delta)$ represents the selectivity in the initial excitation with $0 < \delta < 1$.³² In particular, we may express $\delta = \delta_{\text{imp}} + \delta_{\text{phonon}}$ to account for impurity/defects/substrate-related and phonon-assisted recombination effects that led to intervalley mixing from finite-momentum scattering,³² with $(1 - \delta)$ decreasing with increasing scattering densities and increasing temperature. Thus, from eq 8 we expect P_{circ} to increase with either decrease in τ_{ex} , increase in $\tau_{\text{intervalley}}$, or decrease in δ . For both α - and β -domains of the same h-WS₂ sample, given that they were excited with the same laser power and wavelength, and were also exposed to the same ambient, we may assume that the optically generated exciton densities n_{k}^{ex} and $n_{\text{k}'}^{\text{ex}}$ were the same for both domains.

In monolayer TMDCs at RT, the nonradiative lifetimes may be several orders of magnitude shorter than the radiative

lifetime so that the overall exciton lifetime is much reduced. From our CAFM measurements at rt and using eqs 6 and 7 to fit the PL intensities, we found that the α -domains with lower defect densities would exhibit higher PL intensities and longer nonradiative lifetimes ($\tau_{nr} = 4.7$ ps ~ 10 ps for $n_d = 3.59 \times 10^{10}$ cm $^{-2} \sim 1.49 \times 10^{10}$ cm $^{-2}$), whereas the β -domains with higher defect densities would exhibit lower PL intensities and shorter nonradiative lifetimes ($\tau_{nr} = 1.1$ ps ~ 2.6 ps for $n_d = 1.75 \times 10^{11}$ cm $^{-2} \sim 8.22 \times 10^{10}$ cm $^{-2}$). By considering the radiative (τ_r) and nonradiative (τ_{nr}) lifetimes of excitons in both domains, we could directly estimate the exciton lifetime τ_{ex} by the relation $\tau_{ex}^{-1} = \tau_r^{-1} + \tau_{nr}^{-1}$, which yielded larger values of $\tau_{ex} = 4.72$ ps ~ 10 ps for the α -domains and smaller values of $\tau_{ex} = 1.1$ ps ~ 2.6 ps for the β -domains at RT. Additionally, the large differences in the defect density between the α - and β -domains gave rise to lower selectivity (*i.e.*, smaller $(1-\delta)^2$) in the β -domains. Therefore, the nearly temperature independent P_{circ} in the β -domain may be understood in terms of the competing effects between increasing $(1-\delta)^2$ and decreasing $(\tau_{ex})^{-1}$ with decreasing temperature according to eq 8. In contrast to the β -domain, $(\tau_{ex})^{-1}$ in the α -domain did not decrease as much with decreasing temperature due to far fewer nonradiative recombination sites, whereas the selectivity $(1-\delta)^2$ increased more significantly with decreasing temperature due to diminishing δ_{phonon} and negligible δ_{imp} . Therefore, the value of P_{circ} increased dramatically with decreasing temperature in the α -domains according to eq 8, consistent with our experimental finding.

While the temperature-dependent PL intensities and DOP in both the α - and β -domains of h-WS $_2$ can be consistently explained in terms of the differences in the density of electrically active defects, the microscopic origin for these defects is not yet understood. By performing scanning tunneling microscopy (STM) measurement on monolayer WS $_2$ single crystals,^{55,56} we obtained atomically spatial-resolved images associated with either the SVs (Figure 5a) or the WVs (Figure 5d).

For the SV sites of WS $_2$, as exemplified by the white dash triangles in Figure 5a, the corresponding tunneling conductance spectra were found to be comparable to those of vacancy-free regions. Specifically, both the tunneling current (I) vs bias voltage (V) spectra and the corresponding (dI/dV) vs V spectra taken at a SV (represented by the red curves in Figure 5b,c for the SV location $\alpha 1$ shown in Figure 5a) is essentially indistinguishable from those taken at a vacancy-free region (represented by the orange curves in Figure 5b,c for the vacancy-free location $\alpha 2$ shown in Figure 5a). In particular, the (dI/dV) spectra revealed that the valence band maximum (VBM) and conduction band minimum (CBM) were located at $E_{VBM} \sim -1.1$ eV and $E_{CBM} \sim +0.9$ eV, respectively, yielding a band gap of $E_g = E_{CBM} - E_{VBM} = \sim 2$ eV (Figure 5c). In contrast, for the WV sites as exemplified by the large white dashed triangle in the Figure 5d, the tunneling spectra taken at the WV sites β_1 and β_2 , respectively, illustrated by the blue and green curves in Figure 5e for the I vs V spectra and in Figure 5f for the (dI/dV) vs V spectra, revealed an enhance differential conductance at smaller biased voltages and a smaller bandgap of ~ 1.1 eV, with the VBM and CBM move to ~ -0.8 eV and $\sim +0.3$ eV, respectively. These spectra associated with the WVs were qualitatively similar to the CAFM measurements in Figure 4b, even though direct quantitative comparison of the tunneling conductance data from STM with the contact conductance data derived from CAFM is not straightforward

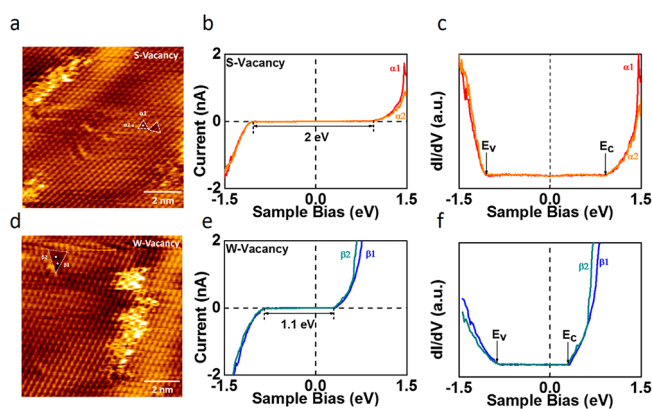


Figure 5. Scanning tunneling microscopic and spectroscopic studies of WS $_2$ monolayer: (a) Atomically resolved of SVs (as indicated by the white triangles) on a sample of monolayer WS $_2$ on Au substrate. The topography was recorded under 0.7 V, 1.2 nA. Here, the white solid circle $\alpha 1$ refers to the location of a SV in the center of a white triangle, and the white solid circle $\alpha 2$ refers to the location of a vacancy-free region. (b) Tunneling current (I) vs sample biased voltage (V) spectra taken at a SV ($\alpha 1$) and defect free region ($\alpha 2$), showing consistent energy gaps of ~ 2.0 eV. Here, the vertical dashed line corresponds to $E = 0$ (the Fermi level). (c) (dI/dV) vs V spectra obtained from the regions $\alpha 1$ and $\alpha 2$ shown in (a). (d) Atomically resolved WVs (shown by the white triangle) on a sample of monolayer WS $_2$ on Au substrate, with the topography recorded under 0.7 V, 1.2 nA. (e) I vs V spectra taken at two WVs (white solid circles $\beta 1$ and $\beta 2$ in (d)), showing a reduced energy gap of 1.1 eV. The vertical dashed line corresponds to $E = 0$ (the Fermi level). (f) (dI/dV) vs V spectra obtained from the regions $\beta 1$ and $\beta 2$ shown in (d). The tunneling spectra associated with the WVs are qualitatively similar to the CAFM measurements at nonradiative defect sites, suggesting that the WVs are responsible for the nonradiative defects that suppress PL and DOP in h-WS $_2$.

without detailed information and modeling of the nanoscale interfacial properties between the AFM tip and WS $_2$. Overall, the combined information derived from atomically resolved STM studies and the nanoscale CAFM measurements strongly suggests that the WV sites rather than the SV sites in monolayer WS $_2$ are the primary nonradiative combination centers that are responsible for the reduction in the PL intensity and DOP.

The aforementioned scenario of a higher WV density in the β -domain is not only consistent with the observation of reduced PL intensities and DOP but also accounts for the larger work function in the β -domain (as found by the KPFM studies) because of the excess hole-doping associated with WVs in WS $_2$. Therefore, we have been able to provide a unified description for the varying chemical, electronic and optical properties of different domains in monolayer h-WS $_2$ in terms of the varying WV densities.

Finally, we note that a well-defined, net valley polarization can be established along the boundary between the α - and β -domains under circularly polarized light as the result of their different DOP. Hence, the domain boundaries in our monolayer h-WS $_2$ samples may be considered as one-dimensional topological channels so that a Hall bar device patterned along one of the domain boundaries is expected to exhibit CPL-induced valley Hall currents even at room temperature. Such opto-valleytronic and related opto-spintronic phenomena for devices fabricated along the topological

channels in monolayer h-WS₂ will be an interesting topic for future investigation.

CONCLUSION

In summary, our experimental investigations based on spatially resolved measurements of PL, Raman spectroscopy, XPS, KPFM, CAFM, and STM have clarified the microscopic physical origin for markedly different reports of PL properties in CVD-grown monolayer WS₂ by attributing the differences to varying densities of tungsten vacancies that act like nonradiative recombination centers. We have also demonstrated large circular polarizations in the PL spectra of our monolayer CVD-grown h-WS₂ single crystals under off-resonant illumination and at relatively high temperatures (from RT to 80 K) when compared with other TMDCs, as detailed in Tables S1 and S2 and summarized in Figure S7. The occurrence of type-two band alignments along the domain walls of h-WS₂ further promises longer exciton lifetimes along the domain boundaries. This work therefore suggests a pathway toward engineering valley polarizations and exciton lifetimes in TMDCs by controlling the type and density of defects that serve as nonradiative exciton recombination sites.

METHODS

Sample Preparation. Pretreatment of SiO₂/Si Substrate. SiO₂/Si substrates (300 nm SiO₂) were used for the CVD growth of WS₂. Prior to the growth, SiO₂/Si substrates were first soaked and sonicated in acetone and isopropyl alcohol (IPA) for 30 min to remove organic impurities, then soaked in Nanostrip for 60 min, and finally washed with deionized water and dried with nitrogen gas.

Synthesis of Mono- and Multilayer WS₂. We used WO₃ and S as precursors in an atmospheric pressure CVD system to grow monolayer h-WS₂ on Si/SiO₂ substrates. A schematic drawing of the home-built CVD system is shown in Figure S1. Our setup includes the following parts: a quartz tube with a diameter of 1 in. and a length of 100 cm, a one-inch inner diameter (i.d.) horizontal split tube furnace (Lindberg Blue M), two mass flow controllers calibrated for Ar and H₂, with stainless steel flanges at both ends connected to a chiller water circulation system operating at 10 °C.

In the first step of the procedure, 95 mg of WO₃ precursor mixed with 5 mg of KI was placed in a quartz boat containing the SiO₂/Si substrates set face-down directly above the W source precursor, and the quartz boat was then positioned at the center of the furnace. A second boat containing 100 mg S (Alfa Aesar, 99.999+%) was placed upstream at 16 cm away from the W source. Next, the system was pumped down to 3 × 10⁻² Torr to eliminate air and moisture. After the system reached the base pressure, the Ar/H₂ (80/40 sccm) carrier gas was introduced until atmospheric pressure was achieved. The furnace was then heated up with a ramp rate of 35 °C/min to the growth temperatures (750 to 850 °C). The Sulfur component melted at 150 °C was sent into the furnace at the growth temperature to grow h-WS₂. The sample growth procedure proceeded for 10 min, after which the furnace was directly opened to room temperature to stop the reaction immediately.

Transfer of Mono- and Multilayer WS₂. Polystyrene (PS) was used as the supplementary film to peel off the WS₂ crystals from silicon substrates. PS (MW 192000) dispersed in toluene solution (20 mg/mL) was spin-coated on top of the WS₂ sample at a speed of 3000 rpm. The edge of the PS film was scribed with a blade, and then the sample of PS/h-WS₂/Si-substrate was inserted into water slowly. The PS/h-WS₂ film became peeled off naturally in water and was subsequently rinsed with deionized-water three times before it was picked up and placed onto the target substrate. The PS coating was removed with toluene after baking the sample at 80 °C for 60 min.

Characterizations by Atomic Probe Microscopy and Kelvin Probe Force Microscopy. Atomic force microscopy (AFM) (Bruker Dimension Icon) under the tapping mode was applied to

characterize the surface morphology of the WS₂ film transferred onto the SiO₂/Si substrate. The KPFM measurements were conducted on a Bruker Dimension Icon SPM. Doped silicon PFQNE-AL probes (Bruker) with a probe radius of 5 nm and a spring constant of 0.8 N/m were used for the electrical measurements.

Spectroscopic Characterization. The quality of the WS₂ film was characterized using Raman spectroscopy, PL measurements, XPS, and UPS. The Raman spectra were taken with a Renishaw M1000 and Renishaw InVia Raman spectrometer system using a 514.3 nm laser (2.41 eV) as the excitation source. A 50× objective lens with a numerical aperture of 0.75 and a 2400 lines/mm and 1800 lines/mm grating were chosen during the measurement to achieve better signal-to-noise ratio. XPS and UPS studies were performed under ultrahigh vacuum (residual gas pressure 5 × 10⁻⁹ Torr) with a Kratos AXIS Ultra DLD and a magnetic immersion lens that consisted of a spherical mirror and concentric hemispherical analyzers with a delay-line detector (DLD). An Al Kα (1.486 keV) monochromatic source and He I (21.2 eV) source were used as excitation sources for the XPS and UPS measurements, respectively. Ejected electrons were collected at a 90° angle from the horizontal. The time-resolved PL measurements were taken on an inverted microscope (Zeiss Axio Observer) equipped with an avalanche photodiode (Picoquant PDM series with PicoHarp 300 timing electronics). For the PL lifetime measurements, a 400 nm picosecond laser diode (70 ps pulse duration, 40 MHz repetition rate; PicoQuant) excitation source was used, and a 400 nm band-pass filter was placed after laser source to purify the laser beam. A 100× objective lens with a numerical aperture of 0.9 (Zeiss, Inc.) was used to focus the pulsed laser to a small spot of 1.6 × 10⁻⁶ cm² with an estimated peak power density of 7.5 kW cm⁻².

STM/STS Sample Preparation and Measurements. For the STM/STS studies, we transferred many flakes of WS₂ (with lateral dimensions of all grains greater than 10 μm) onto a commercial substrate with an atomic flat layer of Au (111) (200 nm thick) on mica so that the surface of the Au (111)/mica substrate was almost fully covered by monolayer WS₂ single crystals. The WS₂/Au (111)/mica sample was annealed and sealed in vacuum, and then loaded onto our Omicron VT STM system. The base pressure of the system was 2 × 10⁻¹¹ Torr. Atomically resolved topographic and spectroscopic measurements were carried out on monolayer WS₂ samples at room temperature using a Pt/Ir STM tip.

ASSOCIATED CONTENT

Supporting Information

The Supporting Information is available free of charge on the ACS Publications website at DOI: 10.1021/acsnano.9b05550.

Supporting Information Note 1 and Figures S1 and S2: CVD synthesis of monolayer WS₂ single crystals. Note 2 and Figure S3: characteristic Raman mode associated with defects/disorder in monolayer WS₂ single crystals. Note 3 and Figure S4: XPS and UPS surface characterizations of WS₂ single crystals. Note 4 and Figure S5: circularly polarized emission from as-grown monolayer h-WS₂ under σ₋ 514.3 nm excitation. Note 5 and Figure S6: circularly polarized emission from as-grown monolayer triangular shape WS₂ under σ₊ 514.3 nm excitation. Note 6: theoretical derivations for the circular polarization P_{circ} of neutral excitons in the steady-state rate model. Note 7, Tables S1 and S2, and Figures S7: summary of the degree of polarization in MoS₂ and WS₂ at room temperature and low temperatures. (PDF)

AUTHOR INFORMATION

Corresponding Author

*E-mail: ncye@caltech.edu.

ORCID 

Wei-Hsiang Lin: 0000-0003-0037-1277

Harry A. Atwater: 0000-0001-9435-0201

Nai-Chang Yeh: 0000-0002-1826-419X

Author Contributions

W.-H.L. and N.-C.Y. conceived the research ideas. W.-H.L. constructed the CVD system for h-WS₂ growth and participated in all of the measurements and data analysis. W.-S.T. contributed to the XPS measurements. C.M.W. and H.A.A. contributed to the TRPL measurement. G.R.R. contributed to the Raman and PL mapping measurements. W.-H.L. and H.A.A. contributed to the STM/STS studies presented in this manuscript using an Omicron VT STM system. M. L. Teague contributed to the STM/STS studies with a homemade STM system in N.-C.Y.'s group to independently verify the STM/STS results obtained by the Omicron VT STM system. W.-H.L. and N.-C.Y. wrote the manuscript, and N.-C.Y. supervised and coordinated the project.

Notes

The authors declare no competing financial interest.

ACKNOWLEDGMENTS

We gratefully acknowledge joint support from the Army Research Office under the Multi-University Research Initiative (MURI) program, National Science Foundation under the Physics Frontier Center program for Institute for Quantum Information and Matter (IQIM), and the Kavli Foundation. We thank Teddy Huang from the Bruker Nano Surface Company for helpful input regarding the CAFM data analysis and Yen-Chun Chen for useful discussions on the CVD growth for TMDCs. We also acknowledge support from the Beckman Institute at the California Institute of Technology for access to facilities at the Molecular Materials Research Center.

REFERENCES

- (1) Novoselov, K. S.; Jiang, D.; Schedin, F.; Booth, T. J.; Khotkevich, V. V.; Morozov, S. V.; Geim, A. K. Two-Dimensional Atomic Crystals. *Proc. Natl. Acad. Sci. U. S. A.* **2005**, *102*, 10451–10453.
- (2) Novoselov, K. S.; Mishchenko, A.; Carvalho, A.; Neto, A. H. C. 2D Materials and van der Waals Heterostructures. *Science* **2016**, *353*, 6298.
- (3) Mas-Balleste, R.; Gomez-Navarro, C.; Gomez-Herrero, J.; Zamora, F. 2D Materials: To Graphene and Beyond. *Nanoscale* **2011**, *3*, 20–30.
- (4) Wang, F.; Wang, Z. X.; Yin, L.; Cheng, R. Q.; Wang, J. J.; Wen, Y.; Shifa, T. A.; Wang, F. M.; Zhang, Y.; Zhan, X. Y.; He, J. 2D Library Beyond Graphene and Transition Metal Dichalcogenides: AFocus on Photodetection. *Chem. Soc. Rev.* **2018**, *47*, 6296–6341.
- (5) Geim, A. K.; Novoselov, K. S. The Rise of Graphene. *Nat. Mater.* **2007**, *6*, 183–191.
- (6) Novoselov, K. S. Nobel Lecture: Graphene: Materials in the Flatland. *Rev. Mod. Phys.* **2011**, *83*, 837–849.
- (7) Sheng, Y. W.; Rong, Y. M.; He, Z. Y.; Fan, Y.; Warner, J. H. Uniformity of Large-Area Bilayer Graphene Grown by Chemical Vapor Deposition. *Nanotechnology* **2015**, *26*, 395601.
- (8) Boyd, D. A.; Lin, W.-H.; Hsu, C.-C.; Teague, M. L.; Chen, C. C.; Lo, Y. Y.; Chan, W. Y.; Su, W. B.; Cheng, T. C.; Chang, C. S.; Wu, C.-I.; Yeh, N.-C. Single-Step Deposition of High-Mobility Graphene at Reduced Temperatures. *Nat. Commun.* **2015**, *6*, 6620.
- (9) Lin, W.-H.; Chen, T. H.; Chang, J. K.; Taur, J. I.; Lo, Y. Y.; Lee, W. L.; Chang, C. S.; Su, W. B.; Wu, C.-I. A Direct and Polymer-Free Method for Transferring Graphene Grown by Chemical Vapor Deposition to Any Substrate. *ACS Nano* **2014**, *8*, 1784–1791.
- (10) Gao, T.; Song, X. J.; Du, H. W.; Nie, Y. F.; Chen, Y. B.; Ji, Q. Q.; Sun, J. Y.; Yang, Y. L.; Zhang, Y. F.; Liu, Z. F. Temperature-Triggered Chemical Switching Growth of In-Plane and Vertically Stacked Graphene-Boron Nitride Heterostructures. *Nat. Commun.* **2015**, *6*, 6835.
- (11) Dean, C. R.; Young, A. F.; Meric, I.; Lee, C.; Wang, L.; Sorgenfrei, S.; Watanabe, K.; Taniguchi, T.; Kim, P.; Shepard, K. L.; Hone, J. Boron Nitride Substrates for High-Quality Graphene Electronics. *Nat. Nanotechnol.* **2010**, *5*, 722–726.
- (12) Ci, L.; Song, L.; Jin, C. H.; Jariwala, D.; Wu, D. X.; Li, Y. J.; Srivastava, A.; Wang, Z. F.; Storr, K.; Balicas, L.; Liu, F.; Ajayan, P. M. Atomic Layers of Hybridized Boron Nitride and Graphene Domains. *Nat. Mater.* **2010**, *9*, 430–435.
- (13) Kim, K. K.; Hsu, A.; Jia, X. T.; Kim, S. M.; Shi, Y. S.; Hofmann, M.; Nezich, D.; Rodriguez-Nieva, J. F.; Dresselhaus, M. S.; Palacios, T.; Kong, J. Synthesis of Monolayer Hexagonal Boron Nitride on Cu Foil Using Chemical Vapor Deposition. *Nano Lett.* **2012**, *12*, 161–166.
- (14) Lin, W.-H.; Brar, V. W.; Jariwala, D.; Sherrott, M. C.; Tseng, W.-S.; Wu, C.-I.; Yeh, N.-C.; Atwater, H. A. Atomic-Scale Structural and Chemical Characterization of Hexagonal Boron Nitride Layers Synthesized at the Wafer-Scale with Monolayer Thickness Control. *Chem. Mater.* **2017**, *29*, 4700–4707.
- (15) Fang, H.; Chuang, S.; Chang, T. C.; Takei, K.; Takahashi, T.; Javey, A. High-Performance Single Layered WSe₂p-FETs with Chemically Doped Contacts. *Nano Lett.* **2012**, *12*, 3788–3792.
- (16) Wang, H.; Yu, L. L.; Lee, Y. H.; Shi, Y. M.; Hsu, A.; Chin, M. L.; Li, L. J.; Dubey, M.; Kong, J.; Palacios, T. Integrated Circuits Based on Bilayer MoS₂ Transistors. *Nano Lett.* **2012**, *12*, 4674–4680.
- (17) Zeng, H. L.; Dai, J. F.; Yao, W.; Xiao, D.; Cui, X. D. Valley Polarization in MoS₂ Monolayers by Optical Pumping. *Nat. Nanotechnol.* **2012**, *7*, 490–493.
- (18) Jones, A. M.; Yu, H. Y.; Ghimire, N. J.; Wu, S. F.; Aivazian, G.; Ross, J. S.; Zhao, B.; Yan, J. Q.; Mandrus, D. G.; Xiao, D.; Yao, W.; Xu, X. D. Optical Generation of Excitonic Valley Coherence in Monolayer WSe₂. *Nat. Nanotechnol.* **2013**, *8*, 634–638.
- (19) He, Z. Y.; Sheng, Y. W.; Rong, Y. M.; Lee, G. D.; Li, J.; Warner, J. H. Layer-Dependent Modulation of Tungsten Disulfide Photoluminescence by Lateral Electric Fields. *ACS Nano* **2015**, *9*, 2740–2748.
- (20) Kim, I. S.; Sangwan, V. K.; Jariwala, D.; Wood, J. D.; Park, S.; Chen, K. S.; Shi, F. Y.; Ruiz-Zepeda, F.; Ponce, A.; Jose-Yacamán, M.; Dravid, V. P.; Marks, T. J.; Hersam, M. C.; Lauhon, L. J. Influence of Stoichiometry on the Optical and Electrical Properties of Chemical Vapor Deposition Derived MoS₂. *ACS Nano* **2014**, *8*, 10551–10558.
- (21) Han, H. V.; Lu, A. Y.; Lu, L. S.; Huang, J. K.; Li, H. N.; Hsu, C. L.; Lin, Y. C.; Chiu, M. H.; Suenaga, K.; Chu, C. W.; Kuo, H. C.; Chang, W. H.; Li, L. J.; Shi, Y. M. Photoluminescence Enhancement and Structure Repairing of Monolayer MoSe₂ by Hydrohalic Acid Treatment. *ACS Nano* **2016**, *10*, 1454–1461.
- (22) Li, H.; Tsai, C.; Koh, A. L.; Cai, L. L.; Contryman, A. W.; Fragapane, A. H.; Zhao, J. H.; Han, H. S.; Manoharan, H. C.; Abild-Pedersen, F.; Nørskov, J. K.; Zheng, X. L. Activating and Optimizing MoS₂ Basal Planes for Hydrogen Evolution Through the Formation of Strained Sulphur Vacancies. *Nat. Mater.* **2016**, *15*, 48.
- (23) Jeong, H. Y.; Jin, Y.; Yun, S. J.; Zhao, J.; Baik, J.; Keum, D. H.; Lee, H. S.; Lee, Y. H. Heterogeneous Defect Domains in Single-Crystalline Hexagonal WS₂. *Adv. Mater.* **2017**, *29*, 1605043.
- (24) Lin, Y. C.; Li, S. S.; Komsa, H. P.; Chang, L. J.; Krasheninnikov, A. V.; Eda, G. K.; Suenaga, K. Revealing the Atomic Defects of WS₂ Governing Its Distinct Optical Emissions. *Adv. Funct. Mater.* **2018**, *28*, 1704210.
- (25) Ly, T. H.; Yun, S. J.; Thi, Q. H.; Zhao, J. Edge Delamination of Monolayer Transition Metal Dichalcogenides. *ACS Nano* **2017**, *11*, 7534–7541.
- (26) Sheng, Y. W.; Wang, X. C.; Fujisawa, K.; Ying, S. Q.; Elias, A. L.; Lin, Z.; Xu, W. S.; Zhou, Y. Q.; Korsunsky, A. M.; Bhaskaran, H.; Terrones, M.; Warner, J. H. Photoluminescence Segmentation within Individual Hexagonal Monolayer Tungsten Disulfide Domains Grown

by Chemical Vapor Deposition. *ACS Appl. Mater. Interfaces* **2017**, *9*, 15005–15014.

(27) Kumar, P.; Verma, N. C.; Goyal, N.; Biswas, J.; Lodha, S.; Nandi, C. K.; Balakrishnan, V. Phase Engineering of Seamless Heterophase Homojunctions with Co-Existing 3R and 2H Phases in WS₂ Monolayers. *Nanoscale* **2018**, *10*, 3320–3330.

(28) Kormanyos, A.; Burkard, G.; Gmitra, M.; Fabian, J.; Zolyomi, V.; Drummond, N. D.; Fal'ko, V. k-p Theory for Two-Dimensional Transition Metal Dichalcogenide Semiconductors. *2D Mater.* **2015**, *2*, 022001.

(29) Ulstrup, S.; Katoch, J.; Koch, R. J.; Schwarz, D.; Singh, S.; McCreary, K. M.; Yoo, H. K.; Xu, J. S.; Jonker, B. T.; Kawakami, R. K.; Bostwick, A.; Rotenberg, E.; Jozwiak, C. Spatially Resolved Electronic Properties of Single-Layer WS₂ on Transition Metal Oxides. *ACS Nano* **2016**, *10*, 10058–10067.

(30) Mak, K. F.; He, K.; Shan, J.; Heinz, T. F. Control of Valley Polarization in Monolayer MoS₂ by Optical Helicity. *Nat. Nanotechnol.* **2012**, *7*, 494.

(31) Kioseoglou, G.; Hanbicki, A. T.; Currie, M.; Friedman, A. L.; Gunlycke, D.; Jonker, B. T. Valley Polarization and Intervalley Scattering in Monolayer MoS₂. *Appl. Phys. Lett.* **2012**, *101*, 221907.

(32) Cao, T.; Wang, G.; Han, W. P.; Ye, H. Q.; Zhu, C. R.; Shi, J. R.; Niu, Q.; Tan, P. H.; Wang, E.; Liu, B. L.; Feng, J. Valley-Selective Circular Dichroism of Monolayer Molybdenum Disulphide. *Nat. Commun.* **2012**, *3*, 887.

(33) Yu, T.; Wu, M. W. Valley Depolarization due to Intervalley and Intravalley Electron-Hole Exchange Interactions in Monolayer MoS₂. *Phys. Rev. B: Condens. Matter Mater. Phys.* **2014**, *89*, 205303.

(34) Zhu, C. R.; Zhang, K.; Glazov, M.; Urbaszek, B.; Amand, T.; Ji, Z. W.; Liu, B. L.; Marie, X. Exciton Valley Dynamics Probed by Kerr Rotation in WSe₂ Monolayers. *Phys. Rev. B: Condens. Matter Mater. Phys.* **2014**, *90*, 161302.

(35) Mai, C.; Semenov, Y. G.; Barrette, A.; Yu, Y. F.; Jin, Z. H.; Cao, L. Y.; Kim, K. W.; Gundogdu, K. Exciton Valley Relaxation in a Single Layer of WS₂ Measured by Ultrafast Spectroscopy. *Phys. Rev. B: Condens. Matter Mater. Phys.* **2014**, *90*, 041414.

(36) Kioseoglou, G.; Hanbicki, A. T.; Currie, M.; Friedman, A. L.; Jonker, B. T. Optical Polarization and Intervalley Scattering in Single Layers of MoS₂ and MoSe₂. *Sci. Rep.* **2016**, *6*, 25041.

(37) Wu, S. F.; Huang, C. M.; Aivazian, G.; Ross, J. S.; Cobden, D. H.; Xu, X. D. Vapor-Solid Growth of High Optical Quality MoS₂ Monolayers with Near-Unity Valley Polarization. *ACS Nano* **2013**, *7*, 2768–2772.

(38) Sallen, G.; Bouet, L.; Marie, X.; Wang, G.; Zhu, C. R.; Han, W. P.; Lu, Y.; Tan, P. H.; Amand, T.; Liu, B. L.; Urbaszek, B. Robust Optical Emission Polarization in MoS₂ Monolayers Through Selective Valley Excitation. *Phys. Rev. B: Condens. Matter Mater. Phys.* **2012**, *86*, 081301.

(39) Lagarde, D.; Bouet, L.; Marie, X.; Zhu, C. R.; Liu, B. L.; Amand, T.; Tan, P. H.; Urbaszek, B. Carrier and Polarization Dynamics in Monolayer MoS₂. *Phys. Rev. Lett.* **2014**, *112*, 047401.

(40) Hanbicki, A. T.; Kioseoglou, G.; Currie, M.; Hellberg, C. S.; McCreary, K. M.; Friedman, A. L.; Jonker, B. T. Anomalous Temperature-Dependent Spin-Valley Polarization in Monolayer WS₂. *Sci. Rep.* **2016**, *6*, 18885.

(41) Zhu, B. R.; Zeng, H. L.; Dai, J. F.; Gong, Z. R.; Cui, X. D. Anomalous Robust Valley Polarization and Valley Coherence in Bilayer WS₂. *Proc. Natl. Acad. Sci. U. S. A.* **2014**, *111*, 11606–11611.

(42) Rosenberger, M. R.; Chuang, H. J.; McCreary, K. M.; Li, C. H.; Jonker, B. T. Electrical Characterization of Discrete Defects and Impact of Defect Density on Photoluminescence in Monolayer WS₂. *ACS Nano* **2018**, *12*, 1793–1800.

(43) McCreary, A.; Berkdemir, A.; Wang, J. J.; Nguyen, M. A.; Elias, A. L.; Perea-Lopez, N.; Fujisawa, K.; Kabius, B.; Carozo, V.; Cullen, D. A.; Mallouk, T. E.; Zhu, J.; Terrones, M. Distinct Photoluminescence and Raman Spectroscopy Signatures for Identifying Highly Crystalline WS₂ Monolayers Produced by Different Growth Methods. *J. Mater. Res.* **2016**, *31*, 931–944.

(44) Yu, Y. F.; Yu, Y. L.; Xu, C.; Cai, Y. Q.; Su, L. Q.; Zhang, Y.; Zhang, Y. W.; Gundogdu, K.; Cao, L. Y. Engineering Substrate Interactions for High Luminescence Efficiency of Transition-Metal Dichalcogenide Monolayers. *Adv. Funct. Mater.* **2016**, *26*, 4733–4739.

(45) Ceballos, F.; Bellus, M. Z.; Chiu, H. Y.; Zhao, H. Ultrafast Charge Separation and Indirect Exciton Formation in a MoS₂-MoSe₂ van der Waals Heterostructure. *ACS Nano* **2014**, *8*, 12717–12724.

(46) Wang, H.; Zhang, C.; Rana, F. Ultrafast Dynamics of Defect-Assisted Electron-Hole Recombination in Monolayer MoS₂. *Nano Lett.* **2015**, *15*, 339–345.

(47) Bhanu, U.; Islam, M. R.; Tetard, L.; Khondaker, S. I. Photoluminescence Quenching in Gold - MoS₂ Hybrid Nanoflakes. *Sci. Rep.* **2015**, *4*, 5575.

(48) Tongay, S.; Suh, J.; Ataca, C.; Fan, W.; Luce, A.; Kang, J. S.; Liu, J.; Ko, C.; Raghunathan, R.; Zhou, J.; Ogletree, F.; Li, J. B.; Grossman, J. C.; Wu, J. Q. Defects Activated Photoluminescence in Two-Dimensional Semiconductors: Interplay between Bound, Charged, and Free Excitons. *Sci. Rep.* **2013**, *3*, 2657.

(49) Yuan, L.; Huang, L. B. Exciton Dynamics and Annihilation in WS₂ 2D Semiconductors. *Nanoscale* **2015**, *7*, 7402–7408.

(50) Ceballos, F.; Zhao, H. Ultrafast Laser Spectroscopy of Two-Dimensional Materials Beyond Graphene. *Adv. Funct. Mater.* **2017**, *27*, 2657.

(51) McCreary, K. M.; Currie, M.; Hanbicki, A. T.; Chuang, H. J.; Jonker, B. T. Understanding Variations in Circularly Polarized Photoluminescence in Monolayer Transition Metal Dichalcogenides. *ACS Nano* **2017**, *11*, 7988–7994.

(52) Miller, B.; Steinhoff, A.; Pano, B.; Klein, J.; Jahnke, F.; Holleitner, A.; Wurstbauer, U. Long-Lived Direct and Indirect Interlayer Excitons in van der Waals Heterostructures. *Nano Lett.* **2017**, *17*, 5229–5237.

(53) He, J. Q.; He, D. W.; Wang, Y. S.; Cui, Q. N.; Ceballos, F.; Zhao, H. Spatiotemporal Dynamics of Excitons in Monolayer and Bulk WS₂. *Nanoscale* **2015**, *7*, 9526–9531.

(54) Zhao, P.; Amani, M.; Lien, D. H.; Ahn, G. H.; Kiriya, D.; Mastandrea, J. P.; Ager, J. W.; Yablonovitch, E.; Chrzan, D. C.; Javey, A. Measuring the Edge Recombination Velocity of Monolayer Semiconductors. *Nano Lett.* **2017**, *17*, 5356–5360.

(55) Hanbicki, A. T.; Currie, M.; Kioseoglou, G.; Friedman, A. L.; Jonker, B. T. Measurement of High Exciton Binding Energy in the Monolayer Transition-Metal Dichalcogenides WS₂ and WSe₂. *Solid State Commun.* **2015**, *203*, 16–20.

(56) Amin, B.; Kaloni, T. P.; Schwingenschlögl, U. Strain Engineering of WS₂, WSe₂, and WTe₂. *RSC Adv.* **2014**, *4*, 34561.